Experimental determination of the H($n=3$) density matrix for 80-keV H$^+$ on He

J. R. Ashburn, R. A. Cline, C. D. Stone, P. J. M. van der Burgt,*
W. B. Westerveld,† and J. S. Risley

*Atomic Collisions Laboratory, Department of Physics, North Carolina State University,
Raleigh, North Carolina 27695-8202*

(Received 6 June 1989)

The density matrix is determined for H($n=3$) atoms produced in axially symmetric electron-transfer collisions of 80-keV protons on helium. In the experiment axial or transverse electric fields with respect to the proton beam are applied to the collision region. The intensity and polarization of Balmer-α radiation emitted by the H($n=3$) atoms are measured as a function of the strength of the external electric field. Detailed analysis of the measured optical signals, taking into account the time evolution of the H($n=3$) atoms in the applied electric field, makes it possible to extract the complete density matrix of the H($n=3$) atoms at the moment of their formation, averaged over all impact parameters. Significant improvements in the experimental technique and in the data analysis associated with the fit of the density matrix to the optical signals have eliminated systematic effects that were present in our previous work [Phys. Rev. A **33**, 276 (1986)]. The improvements in the apparatus are as follows: application of electric fields using electrodes with a simple geometry for the axial and transverse orientations that allows accurate calculation of the spatial variation of the electric field inside the collision chamber; use of high-quality optical elements and a rotatable, single-unit design for the polarimeter; automated gas handling for background subtraction; and full computer control of the electric fields, polarimeter, gas handling, and data acquisition. The analysis incorporates the following improvements: hyperfine structure of the H($n=3$) manifold; cascade from the H($n=4$) manifold; nonuniform detection efficiency over the viewing region; and modeling of the nonuniform electric fields, the nonuniform gas density, and the exponential decrease of the proton beam current in the gas cell due to electron transfer. With these improvements the results from axial electric field measurements are in good agreement with results obtained independently from transverse electric fields. Moreover, the extracted density-matrix elements are found to be within their physically meaningful bounds. The major results from 80-keV collisions are that the H($n=3$) density matrix has an average coherence of 81%±1%, an electric dipole moment of 3.50±0.09 a.u., and a first-order moment of the electron current density distribution $\langle (\mathbf{L} \times \mathbf{A})_{z,s} \rangle$ of -0.13 ± 0.02 a.u. Results from a recent calculation show qualitative agreement with the experiment.

I. INTRODUCTION

Recently, refinements were made to an existing experimental apparatus and analysis procedure that had been used to study excited H($n=3$) atoms produced in H$^+$ on He collisions.[1-6] This paper reviews the method employed, emphasizing the improvements made both in the experiment and the analysis. As a demonstration of the method we present our determination of the density matrix for H($n=3$) atoms produced in electron-transfer collisions of 80-keV H$^+$ on He.

Our study of collisionally excited H atoms is concerned not only with determining cross sections for the production of a particular angular momentum eigenstate but, importantly, with coherence information about the collision. Because the angular momentum eigenstates of hydrogen for a particular principal quantum number are nearly degenerate in energy, the coherent excitation of the manifold can be observed experimentally by using external electric fields and observing the radiation emitted from the decaying excited state.

Eck[7] suggested applying an electric field parallel or antiparallel to the beam direction. Differences in the mea-

sured radiation would indicate coherences between states of opposite parity. This idea was used to observe coherence in excited H atoms produced in several different collision systems: H($n=2$) production from beam-foil experiments,[8] H($n=3$) excitation from electron impact,[9] and H($n=2$) excitation in H-He collisions[10,11] and H$^+$-He collisions.[12] We have studied the production of H($n=3$) atoms in collisions of H$^+$ on He. In our initial work[1] we observed a large difference between the optical signals from parallel and antiparallel electric fields, clearly demonstrating that the collisionally produced H($n=3$) atoms possess an electric dipole moment. In subsequent studies[2] transverse electric fields were used. Analysis of the optical signals led to the determination of electronic currents generated in the H atom in the electron-transfer process.

In the experiment a proton beam is fired through a gas cell containing helium, and the electron-transfer process

$$\mathrm{H}^+ + \mathrm{He} \rightarrow \mathrm{H}(n=3) + \mathrm{He}^+$$
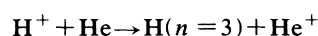
is studied. Axial symmetry applies to the observed transfer process since the scattering angle of the H atom is not observed. The He$^+$ ion is not observed and can be

in any state including the continuum. Because of the implicit experimental averaging over unobserved variables, the experimentally observable coherence of the transfer process is reduced. However, the mixed angular momentum character of the observed process allows some of the coherence to be retained in the averaging and to be observed in the experiment. In such a situation where a statistical mixture of the excited hydrogen atoms is observed, the entire ensemble can be described in terms of a density-matrix formalism expressed in terms of angular momentum eigenstates. The diagonal elements of the density matrix represent the cross sections for electron transfer into different angular momentum eigenstates. The off-diagonal elements represent the coherences for excitation to different angular momentum eigenstates. In the axially symmetric $H(n=3)$ density matrix a total of six independent relative cross sections are determined for electron transfer to the various magnetic sublevels of $H(n=3)$. The coherence of the electron-transfer process is expressed with four independent complex quantities.

Balmer-α radiation emitted by decaying $H(n=3)$ atoms is observed at right angles to the proton beam, as the hydrogen atoms pass within view of the detector. Axial or transverse electric fields applied in the gas cell strongly affect the time evolution of the $H(n=3)$ atoms through Stark mixing. As a consequence, the intensity and polarization of the emitted radiation change substantially depending on the electric field strength and orientation. The intensity and polarization are measured as a function of the electric field strength. Analysis of the optical signals yields the density matrix for the $H(n=3)$ atoms at the moment of their production.

In the analysis of the data the time evolution of the hydrogen atoms is taken into account as they travel along in the external electric field before decaying in view of the detector. Accurate analysis is possible, because the collision process is unaffected by the applied electric field, and because the $H(n=3)$ atoms produced in the collision have virtually the same velocity as the incident protons due to small scattering angles.

In our previous description of the experiment and its analysis,[3] the extracted density matrices exhibited severe inconsistencies due to inadequate analysis of subtle experimental effects. Modifications in the apparatus and in the data analysis have been implemented,[5] resulting in significant improvements in the determination of the density matrices.

The changes in the experimental apparatus and experimental technique include the careful design and construction of the electrodes allowing for accurate determination of the electric fields in the gas cell, a one-piece rotatable Balmer-α polarimeter for the polarization measurements, alternate routing of the gas inlet for accurate measurement of the background signal, suppression of secondary electrons into the Faraday cup, and computer control of all the data-acquisition procedures. The experimental setup now allows the effect of inhomogeneous electric fields to be fully accounted for in the analysis. Also, the effects due to hyperfine interactions, cascade from $H(n=4)$ atoms, nonuniform target-gas density, nonuniform detection efficiency over the viewing region, and ex-

ponential decay of the proton-beam current in the gas cell are incorporated in the analysis. Due to the many improvements in the analysis procedure and in the optical detection system, density-matrix elements obtained from axial field measurements are in overall agreement with elements obtained from transverse electric field measurements. In addition, the results, in general, are physically meaningful in that the diagonal terms are nonnegative and the off-diagonal elements obey the Schwarz inequality.

The purpose of the present paper is to give a synopsis of the complete experimental technique and the analysis procedure, and to discuss the improvements in detail using 80-keV results as an example. Comparison of these results with a recent calculation by Jain, Lin and Fritsch[13] shows qualitative agreement and demonstrates the encouraging progress that has been made in recent years in understanding collisional processes at the intermediate velocities 1–2 a.u.

II. APPARATUS

A. General description

The experimental apparatus has been described before.[3] This section focuses on the improvements. Briefly, positive ions are extracted from a hydrogen arc in a duoplasmatron ion source and accelerated using a 200-kV accelerator. The accelerator power supply is accurate within 0.2%. The ion beam is focused by an electrostatic einzel lens and a quadrupole magnet. Accelerated protons are separated from the positive ion beam using a dipole bending magnet. Three sets of electrostatic steering elements are used for precise positioning of the proton beam. The proton beam is collimated by two 1.6-mm-diam apertures that are placed 26 cm apart, see Fig. 1. After collimation the proton beam passes through the entrance aperture into a differentially pumped gas cell in which helium is admitted to a pressure of about 1 mTorr—a pressure low enough to ensure that the H atoms were formed in single-collision events between protons and He atoms. A shielded Faraday cup biased at +90 V collects the proton beam. Proton currents of about 2 μA are used. Axial or transverse electric fields can be applied inside the gas cell, see Figs. 2 and 3. Radiation, emitted at $90°\pm5°$ to the proton beam ($90°\pm1°$ to the direction of the applied transverse electric field), passes through a vacuum window, a $\lambda/4$ plate, a linear polarizer, and an interference filter, before being detected by a photomultiplier. A double-layer μ-metal shield is used to minimize magnetic fields in the gas cell to less than 5 mG. Motional electric fields experienced by fast hydrogen atoms in the gas cell are negligibly small.[3]

B. Electric fields in the target cell

Within the gas cell electric fields can be applied using one of two arrangements, axial or transverse. Uniform electric fields are simpler to take into account in the analysis described below, but difficult to implement ex-
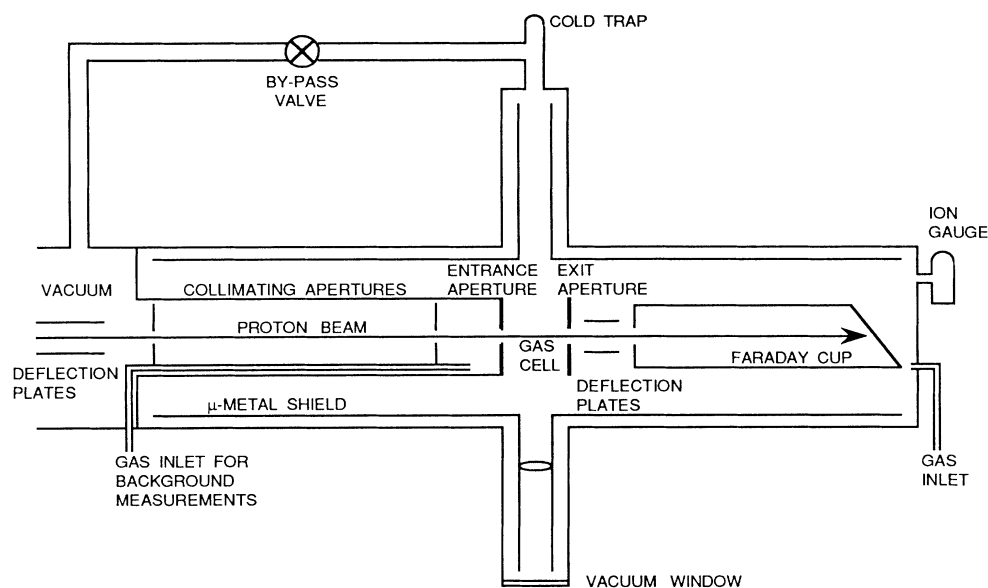
FIG. 1. Schematic overview of the experiment.

perimentally. Instead, a simple electrode geometry was designed and the spatial variation in the electric field is calculated using a relaxation technique. The spatial nonuniformity of the electric field is taken into account in the analysis of the data described in Sec. V.

Axial arrangement. The length of the gas cell is 54.0±0.1 mm and the radius is 38.1 mm. The radius of the entrance aperture is 1.6 mm. The entrance aperture plate is thin, 0.2 mm thick, and provides a sharp edge for the entrance aperture hole. Voltages of equal magnitude, but opposite polarity, are applied to the entrance and to the exit aperture plates. A set of rings between the two plates biased at the appropriate potentials produces a highly uniform electric field along the ion beam axis in the gas cell, see Fig. 2. A circular hole of 10.5 mm radius cut out of the middle of the set of rings allows viewing of the radiation from the excited hydrogen atoms. The resulting distortion in the electric field along the ion-beam

axis caused by this hole is assumed to be negligible.

Some electron-transfer collisions occur immediately outside the gas cell from target gas escaping through the entrance aperture in front of the gas cell. To account for this effect in our analysis, an electrode is placed 12 mm upstream from the entrance aperture with the appropriate potential applied to it to produce an axial electric field in front of the entrance aperture that is nearly the same as that inside the collision region. The distance from the entrance aperture plate to the edge of the ring of the upstream field plate structure is 6.6 mm. The upstream field plate has a large surface area while maintaining a high differential pumping speed near the entrance aperture.

The electric fields are applied using a custom built, precision, 0.01% programmable ±5000-V power supply. The power supply provides equal positive and negative voltages. A voltage divider consisting of 13 equal, pre-
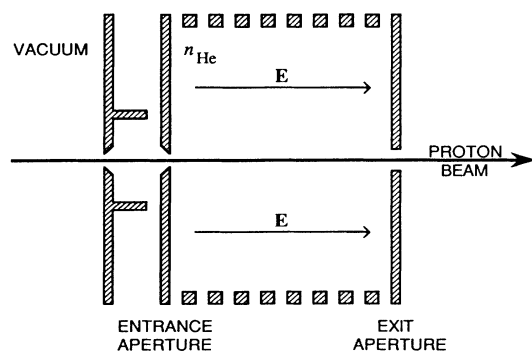

FIG. 2. Geometry for the generation of axial electric fields in the gas cell.
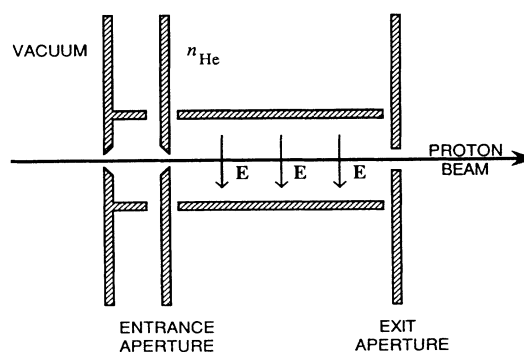

FIG. 3. Geometry for the generation of transverse electric fields in the gas cell.

cision 0.1% resistors is used to divide the potential between the upstream field plate voltage, the entrance aperture plate, the eight defringing rings, and the exit aperture plate. The voltage divider ensures that the potential at the center of the target cell is zero. The potential of each element can be monitored during the experiment. The measured voltages are used to determine the electric field inside the gas cell using the relaxation method. The highest voltage used is 1100 V, providing an electric field strength of 280 V/cm.

The electric field in the gas cell, in the hole of the entrance aperture, and upstream from the entrance aperture is calculated using the relaxation method.[14] The numerical technique utilizes a second-order solution to Laplace's equation and is accurate for electric fields of both low curvature and small gradients, that is, where the fourth-order derivative of the potential is negligible as compared to the second order.

Because of the cylindrical symmetry of the axial electric field, a two-dimensional electric potential with a square grid is used for the relaxation technique. The desired convergence, in the shortest possible computational time, is achieved with three grid densities. A coarse grid of 1×1 mm^2 is used to determine the initial values of the potentials for the interior potentials of the next finer grid. Regions of low field curvature and gradients are determined solely by the coarse grid without any loss of accuracy. It is found that the electric field located well inside the gas cell was 1% smaller than that near the entrance aperture, falling off monotonically. The size of the finest grid is chosen by considering the smallest dimensions associated with the electrodes, that is, the hole in the entrance aperture plate. Since the radius of the aperture is 1.6 mm, a grid dimension one-tenth this size is used, 0.16 mm. For the final results, the finest grid density is iterated 200 times yielding a 0.01% convergence, that is, the maximum difference in any potential after 200 iterations is 0.01% compared to the value after 199 iterations. To check for an unstable plateau in the relaxation technique, it is found that the value for the potential after 200 iterations differs by no more than 0.1% of the value obtained after 100 iterations. It is assumed that the axial electric field is known to an accuracy of 0.2%. The largest uncertainty is the measurement of the inside dimensions of the electrodes.

Transverse electric field: The transverse electric field arrangement, drawn to scale in Fig. 3 has a rectangular electrode. Voltages of opposite polarity are applied to the top and bottom plates which are separated by 20.5 ± 0.1 mm using shielded ceramic spacers to accurately support the plates. The side walls are at ground potential. The applied electric field is perpendicular to both the direction of the ion beam and the direction of the optic axis of the detection system. Light is detected through a hole in one of the side walls. To maintain continuity of the grounded wall, the hole is covered with a tungsten mesh that is 99.8% transparent.

To determine the transverse electric field along the ion beam axis, the relaxation method is used—this time with a three-dimensional cubic grid. The electric potential in the small gaps between the field plates and the adjacent

walls is assumed to vary linearly with distance. The smallest grid size for the transverse electric field is 0.64 mm. Figure 4 shows the calculated transverse electric field strength along the ion-beam axis. It is assumed that the transverse electric field is known to an accuracy of 0.5%.

With this geometrical arrangement the magnitude and the direction of the transverse electric field changes as a function of position along the ion-beam axis because the entrance aperture plate and the walls are at ground potential. The analysis, see Sec. V, assumes that the transverse electric field is pure containing no axial components. The direction of the electric field along the beam axis is exactly perpendicular to the beam. However, the outer edge of the beam experiences a small axial electric field because the electric field lines are bent toward the grounded entrance aperture. The direction of this axial field is in opposite directions for points above and below the beam axis. The axial electric field changes with distance along the proton beam, starting from zero at the aperture rising to a maximum and then tailing off to zero for large distances from the entrance aperture. At the extreme outer edge of the proton beam the largest strength of the axial component has been calculated to be 19% of the nominal transverse field strength. The peak occurs at a position 0.18 cm from the entrance aperture and the full width at half maximum for this axial component is 0.54 cm. The effect of the axial components on the observed signals should be largest for large transverse electric fields. As a check on the assumption that the axial field produces no effect, the density matrix was determined by excluding the highest two and then four electric fields. The density-matrix elements did not change by more than the limits set by the statistical error bars. We conclude that this effect is negligible at 80 keV.

C. Optical system

The optical system is depicted schematically in Fig. 5. Two lenses image a section of the beam on the field stop
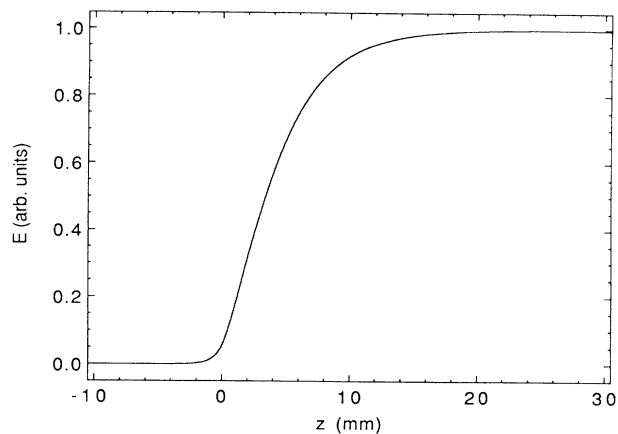

FIG. 4. Normalized transverse electric field strength along the beam axis. The calculation was performed for the set up shown in Fig. 3 using a relaxation technique.
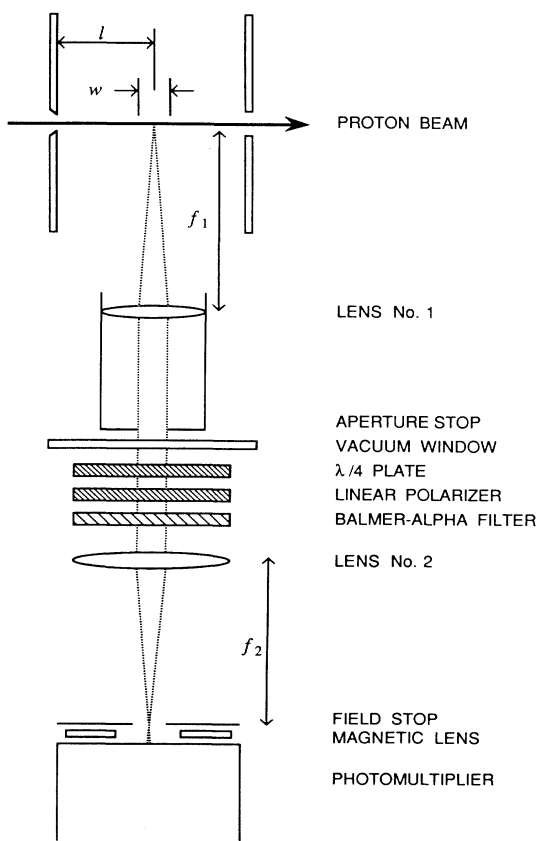
FIG. 5. Schematic overview of the optical system. Measurements are taken as a function of the angle between the optic axis of the $\lambda/4$ plate and the beam axis. The transmission axis of the linear polarizer is kept fixed, parallel to the beam axis.

FIG. 6. A map of the detection sensitivity over the viewing region. The center of the viewing region is located at 24.2±0.1 mm from the entrance aperture for the transverse field setup and at 26.1±0.1 mm for the axial field setup. The full width at half maximum is 6.1±0.1 mm.

in front of the photomultiplier. The intensity and polarization of the emitted radiation are measured using a zeroth-order quartz $\lambda/4$ plate mounted on a motorized rotation stage, followed by a fixed linear polarizer. The quartz $\lambda/4$ plate replaces a mica $\lambda/4$ plate used previously in Ref. 3. The transmission axis of the linear polarizer and the initial orientation of the $\lambda/4$ plate are parallel to the proton beam to within ±1°. An 11-nm bandpass, 656.3-nm interference filter, following the linear polarizer, selects the Balmer-α radiation. The measured retardance of the quartz $\lambda/4$ plate is 88.2°±0.1° at 656.3 nm.[15] This result is used in the analysis of the measured photomultiplier signal.

Both lenses have a focal length of 6.35 cm and the diameter of the aperture stop is 1 cm. Because a section of the beam is viewed, some of the light is incident at a slight angle to the normal of the $\lambda/4$ plate, slightly changing the retardation of the $\lambda/4$ plate. However, the incident angles are small and can be neglected in the analysis.

A map of the detection sensitivity over the viewing region, the section of beam viewed by the optical system, is obtained by moving a light emitting diode mounted on a
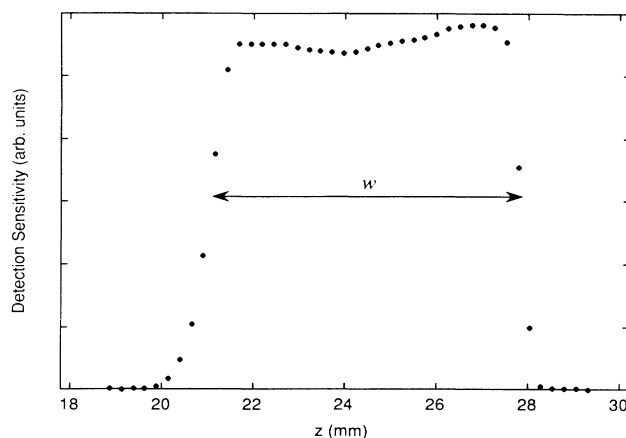
precision linear translator along the beam axis. The relative detection efficiency is found to be uniform to within 4% along a 6.1-mm-long section of beam centered at a distance of 2.42 cm from the entrance aperture for the transverse field setup (2.61 cm for the axial field setup), see Fig. 6. This mapping is used in the analysis in Sec. V.

The $\lambda/4$ plate and the linear polarizer are carefully aligned with respect to the proton beam. The alignment is checked by observing the linear polarization when axial electric fields are applied in the gas cell. Based on our experimental data the $\lambda/4$ plate and the linear polarizer are aligned to about 1° with respect to the proton beam. This alignment could be improved in principle; however, a small misalignment is easily measured and can be corrected for based on the measured photomultiplier signal (see Sec. III A).

The present optical system provides a significant simplification and improvement over the optical system used previously.[3] Because the linear polarizer remains fixed, the light incident on the photomultiplier is linearly polarized parallel to the proton beam, and errors due to the polarization sensitivity of the photomultiplier are eliminated. Polarizing effects of the vacuum window and lenses are found to be negligible.

D. Background subtraction technique

In our measurements, an automated background subtraction technique is employed. Using two small, pneumatically controlled valves, helium from a leak valve can be admitted either to the target chamber, as shown in Fig. 1, for the normal measurement or admitted directly upstream from the entrance aperture for the background measurement. By taking background measurements in this way the experimental conditions upstream from the entrance aperture are kept unchanged from the normal measurement. This method takes into account signals

due to (i) dark counts of the photomultiplier; (ii) light emitted by hydrogen atoms formed in collisions of protons with background gas in the beam line and target area (mostly H_2 from the duoplasmatron source), and (iii) light emitted by hydrogen atoms formed in collisions of protons with helium atoms upstream from the entrance aperture (finite differential pumping ratio). Background typically amounts to about 25% of the total signal. From the obtained corrected signals the Stokes parameters of the emitted light are extracted at each electric field.

The background subtraction technique cannot correct for contributions to the signal from excited H atoms formed in collisions of fast neutral H atoms in the beam with target or background gas. To verify that the contribution in the measured signal from this process is negligible the background pressure upstream from the gas cell was increased by reducing the effective pumping speed. No effect on the measured signal was observed.

E. Microcomputer control

The data-acquisition system is controlled by a microcomputer allowing quick and precise accumulation of data. The main components of the computer controlled system consist of a data-accumulation system, power supplies for the voltages applied to the electric field plates, stepping motor for the rotation of the $\lambda/4$ plate, and the pneumatic valves for the gas-inlet system for background subtraction. The data-accumulation system consists of a charge-sensitive pulse counting system converting photomultiplier pulses into standard transistor-transistor logic (TTL) pulses which are registered in a counter unit. The counter unit consists of a three-channel counter and timer. The signal from the photomultiplier is registered in one of these three channels. The other two channels are used to monitor the proton-beam current and the pressure in the gas cell. The continuous recording of both current and pressure makes normalization of the count rates possible, eliminating the effects of small drifts in the current or the pressure.

III. MEASUREMENT PROCEDURE

A. Stokes parameters and the photomultiplier signal

The coordinate system used in the following analysis is chosen such that the z axis is along the proton beam and the y axis is along the axis of the optical system, see Fig. 7. The radiation emitted along the y axis is completely characterized by its Stokes parameters[16] which are
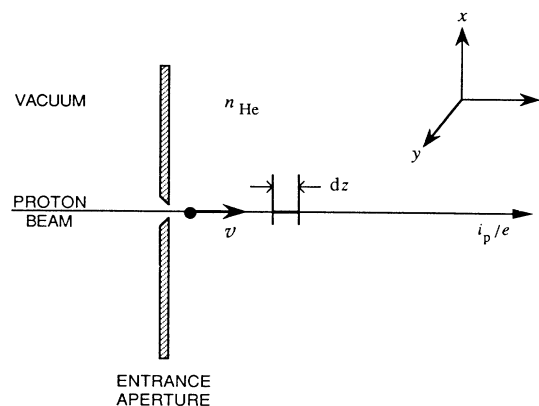

FIG. 7. Protons enter the gas cell with a velocity v along the positive z axis. All along the incident beam excited hydrogen atoms are formed through electron-transfer collisions with helium atoms at number density n_{He}. The hydrogen atoms travel on with the same velocity as the protons. Axial electric fields are applied along the z axis, transverse electric fields along the x axis. Radiation emitted along the positive y axis is detected by the optical system.

defined as follows:

$$S_0 = I_\| + I_\perp ,$$
$$S_1 = I_\| - I_\perp ,$$
$$S_2 = I_{45°} - I_{135°} ,$$
$$S_3 = I_{RH} - I_{LH} ,$$

(3.1)

where $I_\|$ and $I_\perp$ are the intensities for light polarized along the z and x axes, respectively. Similarly, $I_{45°}$ and $I_{135°}$ are the intensities for light polarized at 45° and 135° to the z axis, respectively. I_{RH} and I_{LH} are the intensities for right- and left-hand circular polarization, respectively.

As the intensity of the light detected by the photomultiplier not only depends on the Stokes parameters but also on the angle of the $\lambda/4$ plate, Stokes parameters of the emitted radiation can be extracted from a measurement of the photomultiplier signal as a function of the angle of the $\lambda/4$ plate. The effect of the optical elements on the emitted radiation can be determined through the use of Mueller matrices.[17] The Mueller matrix for the quarter wave plate is

$$\underline{M}_Q(\phi) = \begin{bmatrix} 1 & 0 & 0 & 0 \\ 0 & 1-(1+\delta)\sin^2 2\phi & (1+\delta)\sin 2\phi \cos 2\phi & -\sin 2\phi \\ 0 & (1+\delta)\sin 2\phi \cos 2\phi & 1-(1+\delta)\cos^2 2\phi & \cos 2\phi \\ 0 & \sin 2\phi & -\cos 2\phi & -\delta \end{bmatrix} ,$$

(3.2)

where ϕ refers to the angle that the optic axis of the $\lambda/4$ plate makes with the z axis, and the angle δ is the deviation from 90° of the retardation of the $\lambda/4$ plate. The Mueller matrix for the linear polarizer oriented at 0° with respect to the z axis is

$$\underline{M}_L = \begin{bmatrix} 1 & 1 & 0 & 0 \\ 1 & 1 & 0 & 0 \\ 0 & 0 & 0 & 0 \\ 0 & 0 & 0 & 0 \end{bmatrix} . \qquad (3.3)$$

To find the Stokes parameters for the radiation incident on the photomultiplier, the Stokes vector for the emitted radiation is multiplied with the Mueller matrices:

$$\mathbf{S}' = \underline{M}_L \underline{M}_Q(\phi)\mathbf{S} . \qquad (3.4)$$

The intensity of the radiation incident on the photomultiplier as a function of ϕ is therefore given by

$$S_0'(\phi) = S_0 + S_1 \left[\frac{1-\delta}{2} + \frac{1+\delta}{2}\cos 4\phi \right]$$
$$+ S_2 \frac{1+\delta}{2}\sin 4\phi + S_3 \sin 2\phi . \qquad (3.5)$$

Because of the orientation of the linear polarizer directly in front of the photomultiplier the radiation entering the photomultiplier is always 100% linearly polarized along the z axis and, as a consequence, the photomultiplier signal is directly proportional to $S_0'(\phi)$, independent of the polarization sensitivity of the photomultiplier. The relationship expressed in Eq. (3.5) shows that the Stokes parameters of the emitted radiation can be obtained from a measurement of the photomultiplier signal as a function of ϕ by using linear statistical fitting routines.

Equation (3.5) was derived assuming the optical elements are perfectly aligned with the proton-beam axis. As mentioned in Sec. II C the optical elements are aligned to within ±1° of the beam axis. In addition, it is assumed that the linear polarizer behaves perfectly. Misalignments and imperfect optical elements are systematic effects which are easily accounted for. Their effect on the measured Stokes parameters is discussed in Sec. V C.

B. Data acquisition

The goal of the measurement procedure is to measure the Stokes parameters as a function of the applied electric field strength E. Thirty-seven electric field strengths in the range from zero to 300 V/cm for axial fields and to 400 V/cm for transverse fields are used. Unequal intervals were chosen to best exhibit the expected variation in the Stokes parameters. The measurement is done in two separate parts. In the first part a particular electric field is applied and the signal of the photomultiplier is recorded as a function of the rotation angle ϕ of the $\lambda/4$ plate. The $\lambda/4$ plate is rotated repeatedly over 360° in steps of 7.5°. At each angle the photomultiplier signal is divided by the accumulated current and pressure, thereby eliminating any effects from small drifts in current and pressure. An example of such a measurement is given in Fig. 8. From a least-squares fit of Eq. (3.5) to data of this type
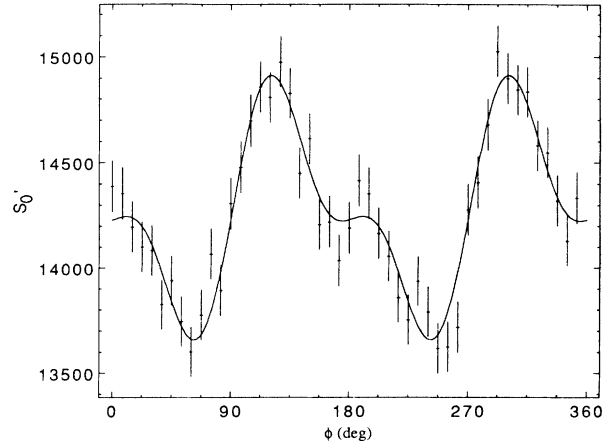

FIG. 8. Measurement of the photomultiplier signal S_0' as a function of the angle ϕ of the $\lambda/4$ plate at a transverse electric field strength of 121.77 V/cm. The error bars represent the statistical uncertainty.

the unnormalized Stokes parameters $\widetilde{S}_i$ and their associated error matrix are extracted at each electric field used. This part of the data acquisition takes about 2 h for each electric field. An entire set of measurements for 37 electric fields takes longer than a week. Since the detection efficiency of our optical system can change by several percent, measurements of $\widetilde{S}_i$ at different electric fields made over the time span of several days must be normalized.

To normalize $\widetilde{S}_i$ the angle of the $\lambda/4$ plate is kept fixed at $\phi = 0°$ and the photomultiplier signal is recorded as a function of applied electric field strength E, providing a relative measurement of $[S_0+S_1]$, the sum of S_0 and S_1, as a function of E. The photomultiplier signal is divided by accumulated current and pressure as before. In addition, measurements at different electric field strengths are interspersed with measurements taken at zero electric field for a common normalization at $E=0$ for all of the $[S_0+S_1]$ measurements. At each electric field the normalized measurement $[S_0+S_1]_{\text{norm}}$ is obtained as

$$[S_0+S_1](E)_{\text{norm}} = \frac{[S_0+S_1](E)}{[S_0+S_1](0)}[S_0+S_1]_{\text{av}}(0) , \qquad (3.6)$$

where $[S_0+S_1]_{\text{av}}(0)$ is the average of the measurements at zero electric field. It takes 10 h to complete the series of $[S_0+S_1]$ measurements at 37 electric fields. When data are accumulated over a short period of time the measured signal shows good repeatability and any variations are within statistical error bars. However, because of the long time it takes to accumulate the $[S_0+S_1]$ measurements, unknown changes in the experiment allow fluctuations in the measured intensity that are outside statistical error bars.

The results obtained in the two series of measurements are combined to provide individual Stokes parameters as a function of E. At each electric field E the normalized Stokes parameters S_i are calculated from

$$S_i = \widetilde{S}_i \frac{[S_0+S_1]_{\text{norm}}}{\widetilde{S}_0 + \widetilde{S}_1} . \qquad (3.7)$$
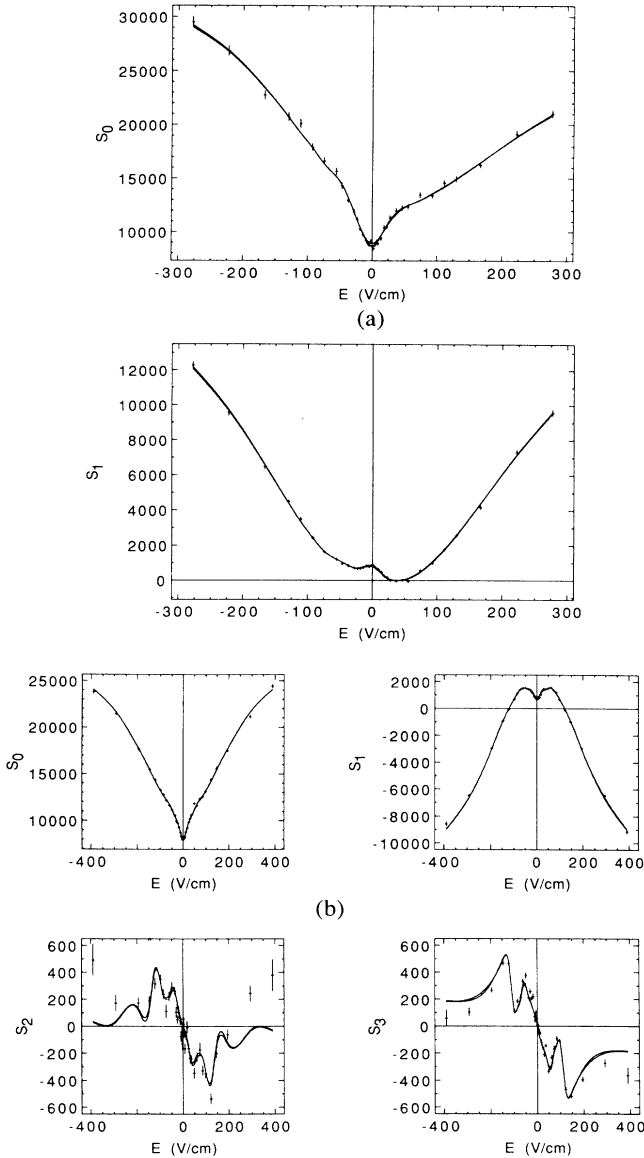
FIG. 9. Measured Stokes parameters for 80-keV H^+ on He collisions. (a) S_0 and S_1 vs axial electric field E. The two lines through the data points represent a simultaneous fit to all of the 80-keV axial data and a simultaneous fit to all of the 80-keV axial and transverse data. The upper curve comes from the axial fit except for small electric field strengths E in the S_0 graph. (b) S_0, S_1, S_2 and S_3 vs transverse electric field E. The two lines through the data points represent a simultaneous fit to all of the 80-keV transverse data and a simultaneous fit to all of the 80-keV axial and transverse data. The upper curve for positive electric field strength E and the lower curve for negative electric field strength E comes from the combined fit.

The Stokes parameters S_i at different electric fields have a common normalization so they can be compared. An example of the measured Stokes parameters as a function of electric field is presented in Fig. 9 for both axial and transverse electric fields.

IV. FORMALISM

A. Time-evolution equation

To obtain information about the electron-transfer process a detailed analysis of the obtained optical data is required. Excited hydrogen atoms are formed all along the proton beam. These atoms evolve in time as they travel on with the speed of the protons. The measured optical data clearly show that the time evolution of the excited atoms can be strongly affected by the applied electric field. In the analysis of the data the time evolution of the formed $H(n=3)$ atoms between the time of production and the time of radiative decay has to be fully accounted for.

Because we observe radiation from a manifold of angular momentum eigenstates, it is advantageous to use a density-matrix formalism. Let $\mathcal{R}_3(z)$ be the number matrix of the excited $H(n=3)$ atoms at position z (see Fig. 7), normalized such that the sum of the diagonal elements represents the number of $H(n=3)$ atoms per unit length of beam. On the basis of the hyperfine angular momentum eigenstates $|\{(l)j\}fm_f\rangle$ the matrix $\mathcal{R}_3(z)$ has dimension 36×36.

The diagonal terms represent the populations per unit length of proton beam of the various angular momentum eigenstates, whereas the off-diagonal elements represent the coherences in the ensemble of atoms. For forward scattering along the z axis the differential equation for $\mathcal{R}_3(z)$ can be written as

$$\frac{d\mathcal{R}_3(z)}{dz}=\frac{-i}{\hbar v}[\mathcal{H}_3(z)\mathcal{R}_3(z)-\mathcal{R}_3(z)\mathcal{H}_3^\dagger(z)]+\frac{1}{v}\frac{\partial\mathcal{R}_3(z)}{\partial t}\ ,$$

(4.1)

where v is the velocity of the $H(n=3)$ atoms. The first term on the right-hand side in Eq. (4.1) represents the time evolution, governed by the phenomenological, electric-field-dependent $H(n=3)$ Hamiltonian $\mathcal{H}_3(z)$. The second term represents the production rate of $H(n=3)$ atoms containing the contribution by direct capture into $H(n=3)$ and the indirect contributions from radiative cascade of $H(n>3)$ to $H(n=3)$:

$$\frac{\partial\mathcal{R}_3(z)}{\partial t}=\left[\frac{\partial\mathcal{R}_3(z)}{\partial t}\right]_{dir}+\left[\frac{\partial\mathcal{R}_3(z)}{\partial t}\right]_{casc}.$$

(4.2)

The direct capture contribution $[\partial\mathcal{R}_3(z)/\partial t]_{dir}$ can be written in terms of the $H(n=3)$ density matrix σ_3,[18]

$$\left[\frac{\partial\mathcal{R}_3(z)}{\partial t}\right]_{dir}=n_{He}(z)\frac{i_p}{e}\sigma_3\ ,$$

(4.3)

where $n_{He}(z)$ is the number density of helium atoms along the proton beam, and i_p/e is the number of protons passing per second through a cross section of the ion beam. In the present experimental situation all the collisionally produced $H(n=3)$ atoms are considered regardless of the impact parameter or azimuthal angle of the capture process. On the basis of the $H(n=3)$ angular momentum eigenstates the diagonal elements of the density matrix σ_3 contain the electron-transfer cross sections

for the various field-free eigenstates. The off-diagonal terms of $\underline{\sigma}_3$ represent the coherences of the capture process between the different eigenstates, averaged over all impact parameters and azimuthal angles. The primary purpose of the present experiment is to access information contained in the density matrix $\underline{\sigma}_3$ to unravel the details of the capture process to H($n=3$).

The rate of indirect production of H($n=3$) atoms depends on the direct capture to H($n>3$) given by the density matrices $\underline{\sigma}_n$ ($n>3$) and the relevant radiative lifetimes and radiative transition elements. The dominant

cascade contribution to $\mathscr{R}_3(z)$ arises from H($n=4$) atoms, which in compact form is given by

$$\left[\frac{\partial \mathscr{R}_3(z)}{\partial t}\right]_{\text{casc}} = \frac{e^2 \omega_{34}^2}{4\pi\epsilon_0 hc^3} \sum_{\varepsilon} \int d\Omega (\varepsilon^* \cdot \mathbf{r}\mathscr{R}_4(z)\mathbf{r} \cdot \varepsilon) \ , \quad (4.4)$$

where ω_{34} is the Paschen-α transition frequency. The summation proceeds over all directions of emission and over a complete set of polarization vectors ε. Matrix elements of $(\partial \mathscr{R}_3(z)/\partial t)_{\text{casc}}$ are given by

$$\left\langle \{(l_3)j_3\}f_3 m_3 \left| \left[\frac{\partial \mathscr{R}_3(z)}{\partial t}\right]_{\text{casc}} \right| \{(l_3')j_3'\}f_3' m_3' \right\rangle$$

$$= \frac{8\pi}{3} \frac{e^2 \omega_{34}^3}{4\pi\epsilon_0 hc^3} \sum_{l_4, l_4'} \sum_{j_4, j_4'} \sum_{f_4, f_4'} \sum_{m_4, m_4'} \langle \{(l_4)j_4\}f_4 m_4 | \mathscr{R}_4(z) | \{(l_4')j_4'\}f_4' m_4' \rangle (-1)^{l_4 + l_4'}(-1)^{j_4 + j_4'}(-1)^{j_3 + j_3'}$$

$$\times (-1)^{m_3 + m_3'}[(2f_3+1)(2f_3'+1)(2f_4+1)(2f_4'+1)(2j_3+1)$$

$$\times (2j_3'+1)(2j_4+1)(2j_4'+1)]^{1/2}\langle l_4 \| \mathbf{r} \| l_3 \rangle \langle l_4' \| \mathbf{r} \| l_3' \rangle$$

$$\times \begin{Bmatrix} f_4 & 1 & f_3 \\ j_3 & i & j_4 \end{Bmatrix} \begin{Bmatrix} f_4' & 1 & f_3' \\ j_3' & i & j_4' \end{Bmatrix} \begin{Bmatrix} j_4 & 1 & j_3 \\ l_3 & s & l_4 \end{Bmatrix} \begin{Bmatrix} j_4' & 1 & j_3' \\ l_3' & s & l_4' \end{Bmatrix}$$

$$\times \sum_q \begin{pmatrix} f_4 & 1 & f_3 \\ m_4 & q & -m_3 \end{pmatrix} \begin{pmatrix} f_4' & 1 & f_3' \\ m_4' & q & -m_3' \end{pmatrix} , \quad (4.5)$$

where $|\{(l_3)j_3\}f_3 m_3\rangle$ and $|\{(l_4)j_4\}f_4 m_4\rangle$ represent the H($n=3$) and H($n=4$) hyperfine angular momentum eigenstates, respectively. The electron and proton spins are denoted by s and i, respectively. In the derivation of Eq. (4.5) the Condon-Shortley phase convention was used for the hydrogen eigenfunctions in which the reduced matrix elements $\langle nl \| \mathbf{r} \| n'l' \rangle$ are real. With this convention the reduced matrix elements $\langle nl \| \mathbf{r} \| n'l' \rangle$ are given by

$$\langle nl \| \mathbf{r} \| n'l' \rangle = (-1)^l [(2l+1)(2l'+1)]^{1/2}$$

$$\times \begin{pmatrix} l & 1 & l' \\ 0 & 0 & 0 \end{pmatrix} \text{Rad}(nl, n'l') \ , \quad (4.6)$$

where $\text{Rad}(nl, n'l')$ represents the radial integrals over the distance r. The differential equation for $\mathscr{R}_4(z)$ has the same form as Eq. (4.1). Explicit solutions of the differential equations Eqs. (4.1)–(4.5) are needed to extract the density matrix $\underline{\sigma}_3$ from the measured optical data.

B. Hamiltonian

A central role in the time evolution is played by the Hamiltonian matrix $\mathscr{H}_3(z)$ which contains electric-field-dependent terms. In the analysis a non-Hermitian Hamiltonian is used to account for loss through radiative decay. The term $\partial \mathscr{R}_3(z)/\partial t$ in Eq. (4.2) only represents the production rate. On the basis of field-free eigenstates $|n\{(l)j\}fm_f\rangle$ the real parts of the diagonal elements give the eigenenergies. In this way fine and hyperfine splittings and Lamb shifts are accounted for implicitly. The radiative decay half widths are included on the diagonal as negative imaginary terms representing radiative loss.[3]

Stark-mixing terms appear as off-diagonal elements in the Hamiltonian. These terms are given by the dot product of the electric field vector $\mathbf{E}$ and the electric dipole operator $e\mathbf{r}$. Matrix elements for the spherical components r_q ($q=1,0,-1$) are given by

$$\langle n\{(l)j\}fm_f | r_q | n\{(l')j'\}f'm_f' \rangle$$

$$= (-1)^l (-1)^{j+j'}(-1)^{s-i+m_f}[(2f+1)(2f'+1)(2j+1)(2j'+1)]^{1/2} \begin{pmatrix} f' & 1 & f \\ m_f' & q & -m_f \end{pmatrix} \begin{Bmatrix} f' & 1 & f \\ j & i & j' \end{Bmatrix}$$

$$\times \begin{Bmatrix} j' & 1 & j \\ l & s & l' \end{Bmatrix} \langle nl \| \mathbf{r} \| nl' \rangle \ , \quad (4.7)$$

where the reduced matrix elements $\langle nl\|\mathbf{r}\|nl'\rangle$ follow from Eq. (4.6).

C. Density matrix

The collisional transfer process to $H(n=3)$ is represented by the density matrix $\underline{\sigma}_3$, which is expressed in terms of hyperfine angular momentum eigenstates and is a 36×36 Hermitian matrix. Several simplifying considerations[5] apply to the density matrix $\underline{\sigma}_3$. The time scales pertaining to the collisional interaction are shorter by several orders of magnitude than those belonging to the subsequent dynamics of the produced hydrogenic system. As a consequence, a clean separation exists between the charge-transfer process and the effects of the atomic time evolution. Because, in addition, the role of the electron and proton spins is insignificant in the transfer process, unpolarized electron and proton spins emerge from the collision, i.e.,

$$\underline{\sigma}_3=\underline{\sigma}_L\otimes\underline{\sigma}_S\otimes\underline{\sigma}_I \ , \tag{4.8}$$

where

$$\underline{\sigma}_S=\underline{\sigma}_I=\begin{bmatrix} \frac{1}{2} & 0 \\ 0 & \frac{1}{2} \end{bmatrix} \tag{4.9}$$

represent the electron- and proton-spin density matrices, respectively. For $H(n=3)$ the density matrix $\underline{\sigma}_L$ expressed in terms of angular momentum eigenstates is a 9×9 matrix which contains on the diagonal the cross sections for electron transfer to the different orbital angular momentum eigenstates $|lm_l\rangle$. In view of Eqs. (4.8) and (4.9) the relationship between the elements of $\underline{\sigma}_3$ and the elements of $\underline{\sigma}_L$ can be specified explicitly by

$$\langle\{(l)j\}fm_f|\underline{\sigma}_3|\{(l')j'\}f'm_f'\rangle=\tfrac{1}{4}\sum_{m_l,m_l'}\sum_{g,m_g}\langle nlm_l|\underline{\sigma}_L|nl'm_l'\rangle(-1)^{l+l'}(-1)^{m_l+m_l'}$$

$$\times(2g+1)[(2f+1)(2f'+1)(2j+1)(2j'+1)]^{1/2}\begin{bmatrix} l & f & g \\ m_l & -m_f & m_g \end{bmatrix}$$

$$\times\begin{bmatrix} l' & f' & g \\ m_l' & -m_f' & m_g \end{bmatrix}\begin{Bmatrix} l & f & g \\ i & s & j \end{Bmatrix}\begin{Bmatrix} l' & f' & g \\ i & s & j' \end{Bmatrix} \ , \tag{4.10}$$

where g and m_g are arbitrary indices.

For the present experimental setup two different spatial symmetries apply to the collisions observed, which restrict the number of independent elements of $\underline{\sigma}_L$. The density matrix $\underline{\sigma}_3$ and, as a consequence, the density matrix $\underline{\sigma}_L$ are invariant for rotations with respect to the proton beam and for reflections with respect to planes containing the proton beam. All the collisions observed are considered regardless of the impact parameter involved. The rotation symmetry requires that

$$\langle nlm_l|\underline{\sigma}_L|nl'm_l'\rangle=\langle nlm_l|\underline{\sigma}_L|nl'm_l'\rangle\delta_{m_lm_l'} \ . \tag{4.11}$$

The reflection symmetry requires that

$$\langle nlm_l|\underline{\sigma}_L|nl'm_l\rangle=\langle n\ l\ -m_l|\underline{\sigma}_L|n\ l'\ -m_l\rangle \ . \tag{4.12}$$

In addition, since $\underline{\sigma}_3$ and $\underline{\sigma}_L$ are Hermitian,

$$\langle nlm_l|\underline{\sigma}_L|nl'm_l\rangle=\langle nl'm_l|\underline{\sigma}_L|nlm_l\rangle^* \ . \tag{4.13}$$

The number of independent real parameters[3] needed to specify $\underline{\sigma}_L$ is reduced to 14 when Eqs. (4.11)–(4.13) are invoked. In Fig. 10 the form of the matrix $\underline{\sigma}_L$ is given based on the angular momentum states $|lm_l\rangle$.

D. Intensity and polarization of the emitted radiation

For a given density matrix $\underline{\sigma}_n$ the set of equations for the number matrix $\underline{\mathcal{R}}_n(z)$ can be solved. The resulting intensity and polarization of light emitted upon radiative decay of the excited hydrogen atoms has to be extracted from the solution for $\underline{\mathcal{R}}_n(z)$ to make a comparison with the optical measurements possible. The intensity $I(\varepsilon;z)$ of Balmer-α radiation of polarization ε emitted per unit length of beam is given by

	s_0	p_{+1}	p_0	p_{-1}	d_{+2}	d_{+1}	d_0	d_{-1}	d_{-2}
s_0	$\sigma_{s_0s_0}$		$\sigma_{s_0p_0}$				$\sigma_{s_0d_0}$		
p_{+1}		$\sigma_{p_{+1}p_{+1}}$				$\sigma_{p_{+1}d_{+1}}$			
p_0	$\sigma_{s_0p_0}^*$		$\sigma_{p_0p_0}$				$\sigma_{p_0d_0}$		
p_{-1}				$\sigma_{p_{-1}p_{-1}}$				$\sigma_{p_{-1}d_{-1}}$	
d_{+2}					$\sigma_{d_{+2}d_{+2}}$				
d_{+1}		$\sigma_{p_{+1}d_{+1}}^*$				$\sigma_{d_{+1}d_{+1}}$			
d_0	$\sigma_{s_0d_0}^*$		$\sigma_{p_0d_0}^*$				$\sigma_{d_0d_0}$		
d_{-1}				$\sigma_{p_{-1}d_{-1}}^*$				$\sigma_{d_{-1}d_{-1}}$	
d_{-2}									$\sigma_{d_{-2}d_{-2}}$

FIG. 10. The $H(n=3)$ density matrix $\underline{\sigma}_L$ on the basis of the $|lm_l\rangle$ angular momentum eigenstates. The elements left blank are zero due to the axial symmetry of the observed collisional phenomenon.

$$I(\varepsilon;z)=\frac{e^2\omega_{23}^3}{4\pi\epsilon_0 hc^3}\sum_{l_2,j_2}\sum_{f_2,m_2}\langle\{(l_2)j_2\}f_2 m_2|\varepsilon^*\!\cdot\!\mathbf{r}\mathcal{R}_3(z)\mathbf{r}\!\cdot\!\varepsilon|\{(l_2)j_2\}f_2 m_2\rangle \tag{4.14}$$

where ω_{23} represents the Balmer-α frequency and $|\{(l_2)j_2\}f_2 m_2\rangle$ represents the angular momentum eigenstates of the H($n=2$) manifold.

Following Nienhuis[19] we define the Cartesian tensor C(z) which gives the intensity of radiation per unit length of beam for any polarization ε,

$$I(\varepsilon;z)=\varepsilon^*\!\cdot\!\mathbf{C}(z)\!\cdot\!\varepsilon\ . \tag{4.15}$$

Multipole components $c_{kq}(z)$ of C(z) ($k=0,1,2$; $q=k,k-1,\ldots,-k$) are defined by

$$\mathbf{C}(z)=\sum_{k,q}c_{kq}(z)\mathbf{S}_{kq}^\dagger\ , \tag{4.16}$$

where the tensors $\mathbf{S}_{kq}$ are given in terms of the spherical unit vectors $\mathbf{e}_\sigma$ ($\sigma=+1,0,-1$) by

$$\mathbf{S}_{kq}=\sum_{\sigma,\sigma'}\mathbf{e}_\sigma\mathbf{e}_{\sigma'}^*(-1)^{1+\sigma+k}\sqrt{2k+1}\begin{bmatrix}1&k&1\\\sigma'&q&-\sigma\end{bmatrix}. \tag{4.17}$$

The multipole components $c_{kq}(z)$ are related to multipole components of the number matrix $\mathcal{R}_3(z)$. The connection is given by (suppressing the z dependence)[3]

$$c_{kq}=\frac{e^2\omega_{23}^2}{4\pi\epsilon_0 hc^3}\sum_{l_2,l_3,l_3'}(-1)^{l_3+l_3'+k+1}\langle l_3\|\mathbf{r}\|l_2\rangle$$
$$\times\langle l_2\|\mathbf{r}\|l_3'\rangle\begin{bmatrix}1&k&1\\l_3&l_2&l_3'\end{bmatrix}$$
$$\times R_{kq}(l_3,l_3')\ , \tag{4.18}$$

where the multipole components $R_{kq}(l_3,l_3')$ are given by

$$R_{kq}(l,l')=\sum_{f,m_f}\sum_{f',m_f'}\sum_{j,j'}(-1)^k(-1)^l(-1)^{j-j'}(-1)^{m_f}[(2f+1)(2f'+1)(2j+1)(2j'+1)(2k+1)]^{1/2}$$
$$\times\begin{Bmatrix}f&k&f'\\j'&i&j\end{Bmatrix}\begin{Bmatrix}j&k&j'\\l'&s&l\end{Bmatrix}\begin{bmatrix}f'&k&f\\m_f'&q&-m_f\end{bmatrix}\langle\{(l')j'\}f'm_f'|\mathcal{R}_3|\{(l)j\}fm_f\rangle\ . \tag{4.19}$$

From the Cartesian form of the tensors $\mathbf{S}_{kq}$ the matrix $\underline{C}$ follows.[20]

As discussed in Sec. IV C, symmetries that apply to the collisional interaction pose restrictions on the elements of the density matrix of the hydrogen atoms at the time of their formation. Likewise symmetries that apply to the subsequent time evolution have their effect on the Stokes parameters of the emitted radiation. Here the direction of the applied electric field is important. In the present experiment the direction of the electric field is always in the x-z plane so that the ensemble of excited hydrogen atoms observed is invariant for reflection with respect to the x-z plane, from which

$$c_{kq}=(-1)^{k-q}c_{k-q}\ . \tag{4.20}$$

The Hermiticity of the number matrix $\mathcal{R}_3(z)$ results in

$$c_{kq}=(-1)^q c_{k-q}^*\ . \tag{4.21}$$

As a consequence, the nine complex c_{kq} are reduced to five independent quantities: c_{00}, c_{20}, c_{21}, and c_{22} are real and c_{11} is purely imaginary. Using explicit expressions for the $\mathbf{S}_{kq}$ from Carrington[20] we find

$$\underline{C}=\begin{bmatrix}\dfrac{\sqrt{2}c_{00}+c_{20}-\sqrt{6}c_{22}}{\sqrt{6}}&0&-c_{11}+c_{21}\\[2mm]0&\dfrac{\sqrt{2}c_{00}+c_{20}+\sqrt{6}c_{22}}{\sqrt{6}}&0\\[2mm]c_{11}+c_{21}&0&\dfrac{c_{00}-\sqrt{2}c_{20}}{\sqrt{3}}\end{bmatrix}. \tag{4.22}$$

Radiation emitted in the y direction can be fully described by the 2×2 x-z submatrix of $\underline{C}$:

$$\underline{c}=\begin{bmatrix}\dfrac{\sqrt{2}c_{00}+c_{20}-\sqrt{6}c_{22}}{\sqrt{6}}&-c_{11}+c_{21}\\[2mm]c_{11}+c_{21}&\dfrac{c_{00}-\sqrt{2}c_{20}}{\sqrt{3}}\end{bmatrix}, \tag{4.23}$$

As discussed in Sec. II C light from atoms at the edge of the viewing region is emitted at a slight angle to the y axis. In this case the polarization vectors ε must be changed accordingly and the corresponding expression is

$$\underline{c} = \begin{vmatrix} \dfrac{\sqrt{2}c_{00} + c_{20} - \sqrt{6}c_{22}}{\sqrt{6}} & (-c_{11} + c_{21})\cos\alpha \\[3mm] (c_{11} + c_{21})\cos\alpha & \dfrac{c_{00} - \sqrt{2}c_{20}}{\sqrt{3}}\cos^2\alpha + \dfrac{\sqrt{2}c_{00} + c_{20} + \sqrt{6}c_{22}}{\sqrt{6}}\sin^2\alpha \end{vmatrix} , \tag{4.24}$$

where α is the angle between the direction of emission and the y axis. In terms of the Stokes parameters of the emitted light the matrix $\underline{c}$ is given by

$$\underline{c} = \frac{1}{2}\begin{vmatrix} S_0 + S_1 & S_2 - iS_3 \\ S_2 + iS_3 & S_0 - S_1 \end{vmatrix} , \tag{4.25}$$

from which the Stokes parameters are deduced in terms of the multipole components c_{kq}.

A number of further symmetries apply, dependent on the configuration used.

(i) Transverse electric fields. A reflection with respect to the y-z plane reverses the transverse electric field and changes the sign of S_2 and S_3. The dependence of S_2 and S_3 on the transverse electric field is therefore antisymmetric, whereas for S_0 and S_1 symmetric behavior results.

(ii) Axial electric fields. For axial electric fields axial symmetry with respect to the z axis is retained. As a result $c_{kq} = 0$ for $q \neq 0$, so that $c_{11} = c_{21} = 0$, and from a comparison of Eqs. (4.23)–(4.25) it follows that $S_2 = S_3 = 0$ for axial electric fields. The dependence of S_0 and S_1 on the axial electric field is in general asymmetric.

A more in-depth analysis[21] shows that even-parity terms of $\underline{\sigma}_L$ have contributions to the different Stokes parameters which are symmetric in the applied electric field; the odd-parity terms contribute in an antisymmetric fashion, regardless of the orientation of the applied electric field.

V. ANALYSIS OF THE DATA

A. Generating the fitting functions

Six independent real diagonal terms and four independent complex off-diagonal terms which characterize $\underline{\sigma}_L$ are extracted from the optical signals. The measured signals are a linear superposition of (hypothetical) signals that would result from each element of $\underline{\sigma}_L$ separately. In other words, the measured Stokes parameters are a linear function of each of the unknown elements of $\underline{\sigma}_L$. Thus the measured Stokes parameters can be written as (assuming no contribution from radiative cascade)

$$S_i^{(a,t)}(E) = \sum_{j,k} f_{ijk}^{(a,t)}(E)\sigma_{jk} , \tag{5.1}$$

where $S_i^{(a,t)}(E)$ represents the ith Stokes parameter measured at an electric field strength E in an axial a or transverse t configuration. The elements of the unknown matrix $\underline{\sigma}_L$ are given by σ_{jk} and the $f_{ijk}^{(a,t)}(E)$ are fitting functions. The fitting functions represent the set of optical signals that would arise from each element of $\underline{\sigma}_L$ separately. A linear statistical fit of the form given in Eq. (5.1) to the data can be used to extract the elements σ_{jk} once the fitting functions are known at each electric field strength E and configurations a and t. To generate the fitting functions $f_{ijk}^{(a,t)}(E)$ the time evolution for $\underline{\mathcal{R}}_3(z)$, Eq. (4.1), is solved numerically for 14 independent basis matrices fully covering the solution space of $\underline{\sigma}_L$.

The electric field strength and the helium number density as a function of z are incorporated in the calculation. The electric field calculation is discussed in Sec. II B. The helium number density $n_{\mathrm{He}}(z)$ along the ion beam is obtained assuming free molecular outflow through the differentially pumped entrance aperture:

$$n_{\mathrm{He}}(z) = \frac{n_0}{2}\left[1 + \frac{z}{(z^2 + r^2)^{1/2}}\right] , \tag{5.2}$$

where the position of the entrance aperture is given by $z = 0$, r is the radius of the entrance aperture, and n_0 represents the helium number density far down stream from the entrance aperture.

To account for these two nonuniformities along the z axis the calculation is performed over a set of small sections of adjustable width. It is assumed that the number densities and electric fields are uniform within the section. The Hamiltonian assigned to a section is diagonalized numerically from which the solution for $\underline{\mathcal{R}}_3(z)$ within a section is readily obtained.[3] The width of a section is adjusted dependent on the local gradients in the number density and the electric field, and is chosen to be small enough to ensure convergence. As an independent check of this approach a separate, much more time consuming, calculation was performed in which a general complex differential equation solver was used. Excellent agreement between the results was found.

The solutions for $\underline{\mathcal{R}}_3(z)$ are used to calculate the multipole components $c_{kq}(z)$, from which the z-dependent intensities and polarization for each nonzero element of $\underline{\sigma}_L$ can be obtained. The fitting functions $f_{ijk}^{(a,t)}(E)$ are obtained by numerically integrating the intensity and polarization over the viewing region.

In a similar way Eq. (4.5) is used to obtain fitting functions $g_{ijk}^{(a,t)}(E)$ for H($n = 4$) terms leading to Balmer-α emission after radiative cascade to H($n = 3$). These calculations are performed neglecting hyperfine structure and assuming uniform helium number densities and electric fields to reduce the CPU time needed for the calculations.

Incoming protons are slightly accelerated or decelerated depending on the direction of the axial field. The kine-

matic effect of the axial field on the energy of the protons is approximated in the calculation by assuming σ_L is unchanged over the resulting ± 1-keV maximum change in proton energy.

B. Statistical fitting of the Stokes parameters

Unconstrained linear fitting of the experimental data is performed to extract the elements of σ_L using the functions $f_{ijk}^{(q,t)}(E)$ and $g_{ijk}^{(q,t)}(E)$ at each electric field strength. Equation (5.1) can be restated in matrix form as

$$\mathbf{S}^{\text{fit}} = \underline{F}\sigma^{\text{col}} , \tag{5.3}$$

where $\mathbf{S}^{\text{fit}}$ represents the fitted value for $\mathbf{S}^{\text{meas}}$, the measured Stokes parameters, $\underline{F}$ is a matrix containing the fitting functions at each electric field used, and σ^{col} is a column vector containing the density-matrix elements. Standard methods[22,23] are used to find $\mathbf{S}^{\text{fit}}$ and σ^{col} from $\mathbf{S}^{\text{meas}}$ and $\underline{F}$. However, correlation between the elements of $\mathbf{S}^{\text{meas}}$ presents added complexity. To solve the problem with correlation we use

$$\chi^2 = \sum_{i,j}(S_i^{\text{meas}} - S_i^{\text{fit}})W_{ij}(S_j^{\text{meas}} - S_j^{\text{fit}}) , \tag{5.4}$$

where

$$\underline{W} = \underline{C}_b^{-1} \tag{5.5}$$

is the weight matrix and $\underline{C}_b$ is the covariance matrix or error matrix between the measured Stokes parameters as discussed below. χ^2 is a minimum when

$$\sigma^{\text{col}} = (\underline{F}^T\underline{W}\,\underline{F})^{-1}\underline{F}^T\underline{W}\,\mathbf{S}^{\text{meas}} \tag{5.6}$$

and

$$\underline{C}_{\sigma^{\text{col}}} = (\underline{F}^T\underline{W}\,\underline{F})^{-1} , \tag{5.7}$$

where $\underline{C}_{\sigma^{\text{col}}}$ is the covariance matrix for the density-matrix elements σ^{col}.

The main improvement in the statistical analysis results from accounting for the propagation of statistical errors in the nonlinear operations expressed in Eqs. (3.5)–(3.7). The analysis takes into account the Poisson statistics associated with the number of counts accumulated at each electric field used. As a result, the covariance matrix between measured Stokes parameters at each electric field is calculated. The covariance matrix contains on the diagonal information about the error in each of the measured Stokes parameters. At each electric field, the matrix used to weight the fit in determining the elements of σ_L is the inverse of the covariance matrix.

To account for error propagation in the nonlinear operations of Eqs. (3.5)–(3.7), we assume that measurements $x_1, \ldots, x_n$ have a statistical covariance matrix $\underline{C}_x$. These measurements are processed to obtain variables $y_1, \ldots, y_m$ from the m equations

$$y_i = f_i(x_1, \ldots, x_n) . \tag{5.8}$$

Elements of the Jacobian matrix $\underline{J}$ for this transformation are given by

$$J_{ij} = \frac{\partial y_i}{\partial x_j} . \tag{5.9}$$

The (asymptotic) covariance matrix $\underline{C}_y$ of the variables $y_1, \ldots, y_m$ is obtained from $\underline{C}_x$ as

$$\underline{C}_y = \underline{J}\underline{C}_x\underline{J}^T . \tag{5.10}$$

In our analysis the covariance matrix $\tilde{C}$ for a set of unnormalized Stokes parameters $\tilde{S}_i$ is a 4×4 matrix. At each electric field E, the measurement $[S_0 + S_1]_{\text{norm}}$ is statistically independent from the four unnormalized Stokes parameters extracted from Eq. (3.5). In the nonlinear operation expressed in Eq. (3.7) these five quantities are reduced to just four, being the normalized Stokes parameters $S_i(E)$ [the operation corresponding to the functions $f_i(x_1, \ldots, x_n)$ introduced above]. The covariance matrix for the normalized Stokes parameters corresponds to the matrix $\underline{C}_y$ introduced above. The covariance matrices for the normalized Stokes parameters are inverted from which the weight matrix is constructed to be used in the fit to determine elements of σ_L.

C. Systematic effects in the measured Stokes parameters

Because of the experimental observation technique certain symmetries related to the orientation of the electric field apply. For axial electric fields the reflection symmetry with respect to the y-z plane requires S_2 and S_3 to be zero. For transverse electric fields a reflection with respect to the y-z plane reverses the electric field and changes the sign of S_2 and S_3. The dependence of S_2 and S_3 on the transverse electric field is therefore antisymmetric whereas the dependence of S_0 and S_1 is symmetric (see Sec. IV D). Because S_3 is more precisely determined than S_2, S_3 more strongly influences the determination of the odd-parity density-matrix elements in the fit.

Because the magnitudes of the S_2 and S_3 Stokes parameters are much smaller (or zero for axial fields) than the S_0 and S_1 parameters, small imperfections in the optical system are most likely to be observed in the measured S_2 and S_3. Indeed, the transverse electric field data for S_2 and S_3 in Fig. 9(b) are not completely antisymmetric.

In particular, the data for S_2 deviates from the fitted line for both small and large electric field strengths. For small electric field strengths the measured S_2 falls slightly below the fitted line. At large electric field strengths there is a distinct positive difference between the measured and fitted S_2. In both cases the deviation is symmetric (i.e., the deviation is the same for $+E$ and $-E$). This systematic effect is caused by the small misalignment of the $\lambda/4$ plate and the linear polarizer discussed in Sec. II C leading to a slight mixture of the measured S_1 and S_2. Figure 9 shows that S_1 is small and positive for small electric field strengths and is large and negative for large electric field strengths. This clearly demonstrates the cause of the small symmetric component of the measured S_1.

The measured data for S_3 also show a symmetric deviation from the fitted line. In this case the deviation is

positive for small electric field strengths and negative for large electric field strengths. Also, the deviation is small at low electric field strengths and is large at high electric field strengths, similar to the symmetric component of the measured S_2. Independent, off-line measurements of the optical system have shown similar effects. This systematic effect cannot, however, be explained by a misalignment of the optical elements. This effect is produced by the imperfect linear polarizer used in the optical system, which transmits slightly elliptically polarized light instead of perfectly linearly polarized light causing a small amount of S_1 to appear as S_3.[24]

Because the S_2 and S_3 measurements for transverse electric fields are fitted to a linear combination of fitting functions that are antisymmetric in the electric field, the results of the fit to the measured Stokes parameters are not affected by the small symmetric components in S_2 and S_3 (see Sec. V B). However, to obtain realistic error estimates for the fitted parameters the measured Stokes parameters S_2 and S_3 are antisymmetrized with respect to the applied transverse electric field.

As an additional cross check, we have measured the polarization of the 728-nm radiation from the He $3\,^1S-2\,^1P$ transition produced in the same collision. Theoretically, the polarization should be zero, however our results indicate $S_1/S_0=0.020\pm0.005$. The cause of this effect is presently unexplained although it may be caused by reflection from metal surfaces outside the gas cell. The 2% polarization is significant in that it is larger than the corresponding $\pm0.5\%$ statistical uncertainty of the Balmer-α radiation signal. However, analysis has shown that most of the density-matrix elements are influenced by less than one standard deviation by this effect.

D. Improvements in the analysis

In the analysis the contribution of cascade from H($n=4$) is taken into account. For a proton energy of 80 keV this contributes as much as a few percent to the measured signals and depends on the electric field strength used. The cascade contribution is relatively small because, at 80 keV, the transit time from the entrance aperture to the end of the viewing region is small compared to the lifetimes encountered in the H($n=4$) manifold. In addition, the limited branching to H($n=3$) and the smaller production cross section relative to H($n=3$) further limit the Balmer-α intensity due to cascade. However, even though the cascade contribution is relatively small its dependence on the electric field strength could possibly affect the results for some of the smaller terms of $\underline{\sigma}_L$.

In principle, one could incorporate the unknown density matrix $\underline{\sigma}_4$ in the statistical analysis but at the cost of a large increase in the number of unknown parameters. Instead, theoretical results are used to set the ratio of H($n=4$) density-matrix elements to the $3s$ density-matrix element.[25] In this way, the dimensionality of the statistical analysis is unchanged. Elements of the H($n=4$) density matrix with $l\leq 1$ are used to correct for cascade. Including the full H($n=4$) density matrix,

which requires substantially more computational time, had no significant effect at 80 keV.

In addition, numerous tests were performed on the analysis to determine which systematic effects were of the greatest importance. Those effects which produced little or no significant change in the density-matrix determination were not included in the final analysis. Some of those effects are small variations in the distance from the entrance aperture to the center of the viewing region, small variations in the size of the viewing region, variation of the detection sensitivity over the viewing region, a 1% decrease in the axial electric field value well within the gas cell, a decrease in the axial electric field inside the entrance aperture, and an exponential decrease in the proton current due to electron transfer inside the gas cell. We have made an effort to include those effects which are most influential in the analysis. Nonetheless, there are some effects that are not included: at lower proton energies, the H atoms are scattered into larger angles; in our analysis we assume that all H atoms are scattered forward with the same velocity as the protons; and the axial component of the electric field in the transverse measurements is ignored.

VI. RESULTS

In Table I, results for 80-keV proton energy are listed, normalized to the s_0 cross section. The listed uncertainties refer to the statistical uncertainty associated with the counting statistics weighted by χ^2. The measurements obtained from the axial and transverse electric field configurations are statistically analyzed separately from each other. The combined results are obtained from a weighted analysis of all the data from both field directions. In addition to the density-matrix elements, values for the average coherence, the electric dipole moment $\langle\mathbf{d}\rangle_z$, a first-order moment of the electron current density distribution $\langle\mathbf{L}\times\mathbf{A}\rangle_{z,s}$, and the reduced χ^2 value from the statistical fit are given. The average coherence is defined as $\mathrm{Tr}(\underline{\sigma}_L^2)$ when $\underline{\sigma}_L$ is normalized such that $\mathrm{Tr}(\underline{\sigma}_L)=1$. This quantity varies between $\frac{1}{9}$ and unity, indicating how closely the density matrix represents a pure state. The large error bars for the average coherence and $\langle\mathbf{L}\times\mathbf{A}\rangle_{z,s}$ in the second column are due to the fact that $\mathrm{Im}(s_0p_0)$ is very weakly determined using axial electric fields. Also shown are our previous experimental results[3] and the results obtained from a microwave resonance technique[26] for the diagonal elements. All of our experimental results can be compared with the recent calculation by Jain, Lin, and Fritsch.[13] Our results for $\langle\mathbf{d}\rangle_z$ and $\langle\mathbf{L}\times\mathbf{A}\rangle_{z,s}$ can be compared with the theoretical results of Jain, Lin, and Fritsch[13] and Burgdörfer and Dubé.[27]

A number of important tests are carried out as a check on the internal consistency of these results. Density-matrix elements are subject to certain constraints by definition. The first constraint is the Schwarz inequality involving the magnitudes of off-diagonal elements and the magnitudes of diagonal elements:

$$|\langle lm|\underline{\sigma}_L|l'm'\rangle|^2\leq\langle lm|\underline{\sigma}_L|lm\rangle\langle l'm'|\underline{\sigma}_L|l'm'\rangle\ .\quad(6.1)$$

TABLE I. Results for the H($n=3$) density matrix from 80-keV proton-helium collision normalized to the 3s cross section. The results from axial and transverse measurements are shown separately, as well as the results from combined fitting of axial and transverse measurements. Also shown are our previous results (Havener), measurements from another experiment (Brower) and recent theoretical calculations by Jain, Lin, and Fritsch and Burgdörfer and Dubé.

Element	Axial	Transverse	Combined	Havener[a]	Brower[b]	Jain, Lin, and Fritsch[c]	Burgdörfer and Dubé[d]
s_0	1.000±0.029	1.000±0.015	1.000±0.010	1.0	1.0	1.0	1.0
p_0	0.159±0.020	0.136±0.019	0.164±0.006	−0.09	0.13±0.01	0.139	
$p_{\pm1}$	0.016±0.006	0.007±0.005	0.005±0.003	0.11	0.025±0.005	0.0118	
d_0	0.038±0.036	0.004±0.011	0.027±0.008	0.04	0.013±0.003	0.012	
$d_{\pm1}$	−0.015±0.026	0.012±0.008	−0.007±0.006	0.03	0.050±0.001	0.002	
$d_{\pm2}$	0.009±0.007	0.007±0.002	0.011±0.001	−0.01	−0.001±0.001	0.00016	
Re($s_0 p_0$)	0.266±0.013	0.266±0.009	0.267±0.008	0.22		0.130	
Im($s_0 p_0$)	−0.32 ±0.59	0.013±0.009	0.019±0.007	0.01		−0.080	
Re($s_0 d_0$)	0.054±0.045	0.079±0.021	0.063±0.010	0.18		0.0133	
Im($s_0 d_0$)	0.05 ±0.15	−0.129±0.050	−0.057±0.028	−0.85		0.0032	
Re($p_0 d_0$)	0.025±0.007	0.031±0.005	0.025±0.002	0.02		0.018	
Im($p_0 d_0$)	0.014±0.008	0.024±0.004	0.015±0.002	0.00		0.025	
Re($p_{\pm1} d_{\pm1}$)	0.005±0.007	0.005±0.002	0.003±0.002	0.00		0.0034	
Im($p_{\pm1} d_{\pm1}$)	0.014±0.009	0.003±0.001	0.003±0.001	0.00		0.0034	
Average coherence	94% ±51%	85.2%±2.7%	81.1%±1.0%	130%		75.1%	
$\langle \mathbf{d} \rangle_z$	3.50±0.13	3.62±0.14	3.500±0.087	2.8		1.83	1.42
$\langle \mathbf{L} \times \mathbf{A} \rangle_{z,s}$	0.7±1.5	−0.153±0.019	−0.128±0.019	0.0		0.105	0.21
χ^2	1.2	1.7	1.2		3.0		

[a] Reference 3.
[b] Reference 26.
[c] Reference 13.
[d] Reference 27.

A second constraint requires that diagonal elements be non-negative:

$$\langle lm \,|\underline{\sigma}_L|\, lm \rangle \geq 0 \ . \tag{6.2}$$

In contrast to our earliest results the present results satisfactorily obey these constraints to within the experimental incertainty. The comparison of our combined results with the earlier results[3] illustrates the progress realized with the recent improvements in the experiment and in the analysis.

Statistical fitting to 14 parameters is easily affected by subtle systematics not incorporated in the analysis, particularly since some parameters are one or two orders of magnitude smaller than the more dominant s_0 parameter. Some of the fitting functions for different elements of $\underline{\sigma}_L$ introduce strong (statistical) correlation between some of the elements making an independent determination of those elements difficult. By measuring all the relevant Stokes parameters in two different electric field configurations this latter problem is minimized. By comparing results obtained independently from the axial and from the transverse field measurements an important test is performed to uncover possible systematic effects. Any systematic in the experiment that is not correctly accounted for in the analysis is unlikely to manifest itself in a similar manner in the two electric field cases. As shown in Table I the results for the two electric field orientations are in overall agreement with each other to within the specified error bars. The results shown in Table I were not repeated to check reproducibility. However, repeated measurements at other proton energies indicate that our results are reproducible to within the error bars shown.

As an additional test, the reduced χ^2 of the simultaneous fit of all the data (axial and transverse field measurements) was calculated based on Poisson counting statistics. Reduced χ^2 values of less than 2 were obtained. This result suggests possible systematics to be of the order of or less than the statistical uncertainties. Because systematics might cause results for individual elements to be biased to a greater extent than suggested by the standard deviations, the error bars given in Table I have been multiplied by $(\chi^2)^{1/2}$. For the combined fit the data from both field directions were weighted by $1/\chi^2$ from the individual fits of axial and transverse data before being combined.

While there have been many measurements on $H(n=3)$ production[3] in proton-helium collisions, we compare our results with experiments that determine cross sections for production of particular m_l levels. In the work of Brower and Pipkin[26] fine structure transitions of the $H(n=3)$ manifold are driven with a microwave field and the resulting effect on the Balmer-α emission is recorded. In this method only information about diagonal density-matrix elements is obtained. No information pertaining to the off-diagonal elements is obtained due to the absence of static fields mixing the angular momentum eigenstates. The comparison with our combined results for the diagonal elements shows a reasonable agreement except for a noticeably different
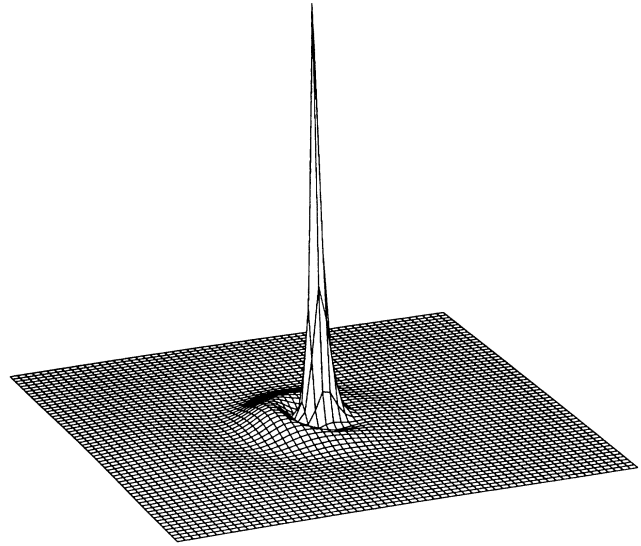

FIG. 11. Electron density distribution of $H(n=3)$ formed in 80-keV collision. The hydrogen atom is traveling to the right. The grid size is 0.5 a.u.

value for the $p_{\pm 1}$ density-matrix element.

Several authors have performed calculations for production of $H(n=3)$ in proton-helium collisions.[13,27,28] We compare our results to those calculations which give information about off-diagonal density-matrix elements. Burgdörfer and Dube[27] have used the continuum distorted-wave approximation with post-collision interaction (CDW-PCI) to calculate the full $H(n=3)$ density
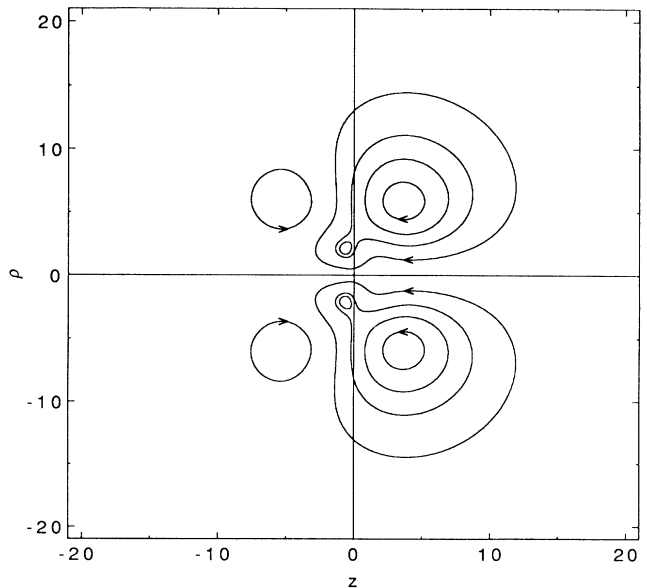

FIG. 12. Current density distribution of $H(n=3)$ formed in 80-keV collision. The axis units are in a.u. The vertical axis represents the distance from the z axis.

matrix. Here we compare our results with their published work for $\langle d \rangle_z$ and $\langle L \times A \rangle_{z,s}$. The most extensive results for the proton-helium system were recently published by Jain, Lin, and Fritsch.[13] These calculations were performed using the AO+ method in which a truncated set of atomic orbital (AO) basis functions is supplemented by pseudofunctions to represent the continuum part of the collision problem. This method breaks down at the lower energies where the molecular character of the collision complex is important. Likewise, in the high energy limit the truncated basis set does not allow accurate results to be obtained. An overall comparison of this calculation with our results at the intermediate energy of 80 keV shows the very similar trends in the two sets of data. However, the actual numerical comparison shows that in particular the $Re(s_0 p_0)$ is substantially too low.

The electron charge distribution[1] for H($n=3$) atoms at the moment of production is shown in Fig. 11 using the density-matrix elements from the combined fit. The graph shows the probability (height) of finding the electron as a function of position in the x-z plane. Figure 12 shows the electron current distribution[2] within H($n=3$) atoms at the moment of production, again using the combined fit.

ACKNOWLEDGMENTS

*Present address: University of Windsor, Windsor, Ontario Canada.

†Permanent address: University of Utrecht, The Netherlands.

[1] C. C. Havener, W. B. Westerveld, J. S. Risley, N. H. Tolk, and J. C. Tully, Phys. Rev. Lett. 48, 926 (1982).

[2] C. C. Havener, N. Rouze, W. B. Westerveld, and J. S. Risley, Phys. Rev. Lett. 53, 1049 (1984).

[3] C. C. Havener, N. Rouze, W. B. Westerveld, and J. S. Risley, Phys. Rev. A 33, 276 (1986). A more complete bibliography of earlier work is presented in this reference.

[4] N. Rouze, C. C. Havener, W. B. Westerveld, and J. S. Risley, Phys. Rev. A 33, 294 (1986).

[5] W. B. Westerveld, J.R. Ashburn, R. A. Cline, C. D. Stone, P. J. M. van der Burgt, and J. S. Risley, Nucl. Instrum. Methods B 24/25, 224 (1987).

[6] W. B. Westerveld, J. R. Ashburn, R. A. Cline, C. D. Stone, P. J. M. van der Burgt, and J. S. Risley, in Correlation and Polarization in Electronic and Atomic Collisions, edited by Albert Crowe and Michael R. H. Rudge (World Scientific, Singapore, 1988), p. 271–302.

[7] T. G. Eck, Phys. Rev. Lett. 31, 270 (1973).

[8] I. A. Sellin, J. R. Mowat, R. S. Peterson, P. M. Griffin, R. Laubert, and H. H. Haselton, Phys. Rev. Lett. 31, 1335 (1973).

[9] R. Krotkov, Phys. Rev. A 12, 1793 (1975).

[10] R. Krotkov and J. Stone, Phys. Rev. A 22, 473 (1980).

[11] Rainer Hippler, in Electronic and Atomic Collisions, edited by H. B. Gilbody, W. R. Newell, F. H. Read, and A. C. H. Smith (North-Holland, Amsterdam, 1988).

[12] Robert DeSerio, Carlos Gonzalez-Lepera, John P. Gibbons, Joachim Burgdörfer, and I. A. Sellin, Phys. Rev. A 37, 4111 (1988).

[13] Ashok Jain, C D. Lin, and W. Fritsch, Phys. Rev. A 35, 3180

(1987); 36, 2041 (1987); 37, 3611(E) (1988). References to earlier theoretical work are included in this reference.

[14] William H. Press, Brian P. Flannery, Saul A. Teulkolsky, and William T. Vetterling, Numerical Recipes (Cambridge University Press, Cambridge, England, 1987), pp. 652–659.

[15] J. R. Ashburn, Ph.D. thesis, North Carolina State University, 1989.

[16] G. G. Stokes, Trans. Cambridge Philos. Soc. 9, 399 (1852).

[17] D. Clarke and J. F. Grainger, Polarized Light and Optical Measurement (Pergamon, Oxford, 1971), pp. 35–39.

[18] The notation used in this article is slightly different than that used in Ref. 3. The number matrix $\mathcal{R}_3$ in this article was called N in Ref. 3 and the density matrix σ_3 was denoted by ρ in Ref. 3.

[19] Gerard Nienhuis, in Coherence and Correlation in Atomic Physics, edited by H. Kleinpoppen and J. F. Williams (Plenum, New York, 1980), pp. 121–132.

[20] C. G. Carrington, J. Phys. B 4, 1222 (1971).

[21] G. Gabrielse, Phys. Rev. A 22, 138 (1980).

[22] S. L. Meyer, Data Analysis for Scientists and Engineers (Wiley, New York, 1975).

[23] Philip R. Bevington, Data Reduction and Error Analysis for the Physical Sciences (McGraw-Hill, New York, 1969).

[24] J. M. M. de Nijs and A. van Silfhout, J. Opt. Soc. Am. A 5, 773 (1988).

[25] Ashok Jain (private communication).

[26] M. C. Brower and F. M. Pipkin, Phys. Rev. A 39, 3323 (1989).

[27] Joachim Burgdörfer and Louis J. Dubé, Nucl. Instrum. Methods B 10/11, 198 (1985); Phys. Rev. Lett. 52, 2225 (1984).

[28] Thomas G. Winter and Chun C. Lin, Phys. Rev. A 10, 2141 (1974).